Check for updates

Downloaded 10/26/20 to 12.233.159.194. Redistribution subject to SEG license or copyright; see Terms of Use at https://library.seg.org/page/policies/terms
DOI:10.1190/INT-2020-0053.1

# Attribute-assisted characterization of basement faulting and the associated sedimentary sequence deformation in north-central Oklahoma

Max Firkins[1], Folarin Kolawole[1], Kurt J. Marfurt[1], and Brett M. Carpenter[1]

## Abstract

Patterns of recent seismogenic fault reactivation in the granitic basement of north-central Oklahoma necessitate an understanding of the structural characteristics of the inherited basement-rooted faults. Here, we focus on the Nemaha Uplift & Fault Zone (NFZ) and the surrounding areas, within which we analyze the top-basement and intrabasement structures in eight poststack time-migrated 3D seismic reflection data sets. Overall, our results reveal 115 fault traces at the top of the Precambrian basement with sub-vertical dips, and dominant trends of west-northwest–east-southeast, northeast–southwest, and north–south. We observe that proximal to the NFZ, faults dominantly strike north–south, are fewer (<10), and have the lowest areal density and intensity, while displaying the largest maximum vertical separation. However, farther away (>30 km) from the NFZ, faults exhibit predominantly northeast–southwest trends, fault areal density and intensity increases, and maximum vertical separation decreases steadily. Of the analyzed faults, approximately 49% are confined to the basement (intrabasement), ~28% terminate within the Arbuckle Group, and approximately 23% transect units above the Arbuckle Group. These observations suggest that (1) proximal to the NFZ, deformation is dominantly accommodated along a few but longer fault segments, most of the mapped faults cut into the sedimentary rocks, and most of the through-going faults propagate farther up-section above the Arbuckle Group; and (2) with distance away from the NFZ, deformation is diffuse and distributed across relatively shorter fault segments, and most basement faults do not extend into the sedimentary cover. The existence of through-going faults suggests the potential for spatially pervasive fluid movement along faults. Further, observations reveal pervasive, subhorizontal intrabasement reflectors (igneous sills) that terminate at the basement-sediment interface. Results have direct implications for wastewater injection and seismicity in north-central Oklahoma and southern Kansas. Additionally, they provide insight into the characteristics of basement-rooted structures around the NFZ region and suggest a means by which to characterize basement structures where seismic data are available.

## Introduction

The U.S. Midcontinent region has experienced an increase in seismicity, starting in 2009 and spiking in 2016, with many of these events concentrated in Oklahoma (Figure 1a) (e.g., Jacobs, 2016). The bulk of these earthquakes has occurred in the crystalline basement on previously unmapped faults (e.g., Kolawole et al., 2019). Across this region, the Precambrian basement mostly is buried (Sims, 1985); thus, the detailed structure and characteristics of the basement which make it susceptible to seismogenic reactivation remain poorly understood. Fracture systems mapped in the field on limited basement exposures in southern Oklahoma have been correlated with trends of observed seismicity across the region (Kolawole et al., 2019; Qin et al., 2019). However, there remains the need to characterize basement structures in the north-central Oklahoma region where seismicity is most frequent. Presently, the Ordovician-age carbonate Arbuckle Group is of interest in Oklahoma because it represents the disposal unit for the increased volumes of produced wastewater from hydrocarbon exploration activities (e.g., Kroll et al., 2017; Yeck et al., 2017; Kolawole et al., 2019). Injection into this unit has been linked to the increased levels of seismicity within the state. It is assumed that the pervasive presence of faults, which connect the basement and sedimentary cover, would increase the likelihood of fluid movement between the sedimentary injection zones and the basement (e.g., Mohammadi et al., 2019). To date, the relative proportions of the basement-rooting faults that cut into and through the Arbuckle unit and shallower units are not known. Although the cause of the recent seismicity is likely related to a combination of poroelastic loading and

[1]University of Oklahoma, School of Geosciences, RM 710, Sarkeys Energy Center, 100 East Boyd Street, Norman, Oklahoma 73019-0390, USA. E-mail: max_firkins@ou.edu (corresponding author); folarin@ou.edu; kmarfurt@ou.edu; brett.carpenter@ou.edu.

Manuscript received by the Editor 2 February 2020; revised manuscript received 29 May 2020; published ahead of production 10 August 2020; published online 26 October 2020. This paper appears in *Interpretation*, Vol. 8, No. 4 (November 2020); p. SP175–SP189, 8 FIGS.
http://dx.doi.org/10.1190/INT-2020-0053.1. © 2020 Society of Exploration Geophysicists and American Association of Petroleum Geologists. All rights reserved.

Downloaded 10/26/20 to 12.233.159.194. Redistribution subject to SEG license or copyright; see Terms of Use at https://library.seg.org/page/policies/terms
DOI:10.1190/INT-2020-0053.1

pore-pressure diffusion (e.g., Chang and Segall, 2016; Zhai et al., 2019), it is envisioned that the transmission of produced water into the basement is likely to alter the mineralogy and, potentially, the stress state in the crystalline basement (e.g., Qin et al., 2019). This could lead to delayed and long-lived seismicity within the region (Pollyea et al., 2019).

In this study, we analyze seismic data from two counties in north-central Oklahoma (Figure 1a and 1b) to identify structures that are present within the crystalline basement, the characteristics of their propagation into the sedimentary cover, and their relationship with patterns of seismicity in the region. Our analyses will show that the salient, first-order structural characteristics of the intrabasement and basement-rooted structures in north-central Oklahoma and elucidate the implications for fluid injection-related seismicity in the region.

## Geologic setting

### *The Precambrian igneous basement of north-central Oklahoma*

In the area of interest for this study, the granitic basement has been shown to vary compositionally and texturally (Denison, 1966, 1981; Shah and Keller, 2017). It has been shown in prior work that the crystalline basement in Oklahoma and large portions of the central U.S. are comprised of the Southern and Eastern Granite-Rhyolite Provinces (Bickford et al., 1981; Anderson, 1983; Thomas et al., 1984; Lidiak, 1996; Bickford et al., 2015). They intruded into the preexisting Yavapai and Mazatzal accretionary terranes of the North American Continent (Anderson, 1983). There is some debate as to the exact process of formation; however, there appears to be a consensus that in general, the development of the provinces is related to large-scale continental extension/rifting (Slagstad et al., 2009).

### *Tectonic history of the region*

Within the present-day state of Oklahoma, several major Precambrian structures have been identified, including the Midcontinent Rift, Nemaha Fault Zone (NFZ), Labette Fault, and Osage Dome (e.g., Figure 1a–1c; Denison, 1981; Stein et al., 2014). The largest of these is the Midcontinent Rift and the NFZ. The NFZ is a prominent feature in the U.S. Midcontinent. The structure trends north-northeast–south-southeast stretching for approximately 650 km through present-day Nebraska, Kansas, and Oklahoma (McBee, 2003). Although its origin still is indeterminate, evidence of normal, strike-slip, and reverse faulting is observed. Hypotheses as to the fault zone's origins include wrench faulting associated with the Taconic Orogeny (McBee, 2003) or thrust faulting due to successive compressional events (Gay, 2003).

Basement-involved Phanerozoic deformation in Oklahoma is attributed to three major tectonic events: one extensional and two orogenic, all in the south (Figure 1c). Temporally, the Southern Oklahoma Aulacogen (SOA) formed earliest during the Middle to Late Cambrian

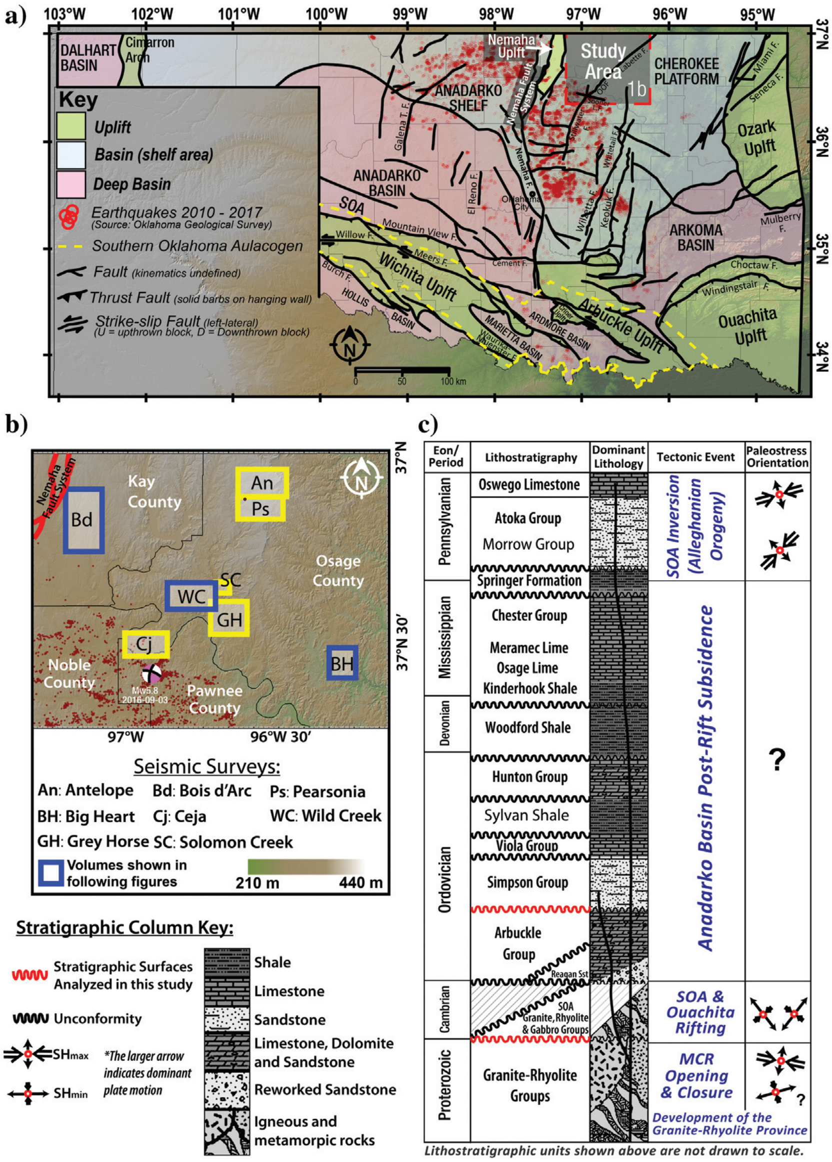


**Figure 1.** The geologic and neoseismic setting of the study area: (a) tectonic map of Oklahoma showing the geologic provinces (modified after Northcutt and Campbell, 1995; Kolawole et al., 2020). The red dashed square shows the location of the study area. (b) Digital elevation model hillshade map of the study area in north-central Oklahoma, showing the location of the eight 3D seismic reflection surveys used in this study. (c) Simplified stratigraphic column of the Anadarko Basin (after Kolawole et al., 2020). The stratigraphic tops in red represent the surfaces of interest in this study.

Downloaded 10/26/20 to 12.233.159.194. Redistribution subject to SEG license or copyright; see Terms of Use at https://library.seg.org/page/policies/terms
DOI:10.1190/INT-2020-0053.1

breakup of Rodinia (Moores, 1991) and the formation of the proto-Atlantic Ocean (Burke and Dewey, 1973). The SOA trends west-northwest–east-southeast and extends aerially across northeastern Texas, southern Oklahoma, and into the north Texas Panhandle (Figure 1a). It then segments and continues across northeastern New Mexico and into the border of central Colorado and Utah (Keller and Stephenson, 2007). Thermal subsidence followed the failure of the SOA rift arm, creating accommodation for early phanerozoic sediment deposition (Perry, 1989).

In late Mississippian time, the collision of Laurentia and Gondwana began (Hatcher, 2010). The collision of these continents, known as the Alleghenian Orogeny, created the Appalachian, Ouachita, and Marathon fold-thrust belts affecting much of the eastern and southeastern United States (Figure 1c). This orogenic event was long-lived and is responsible for the reactivation of numerous structures, including portions of the SOA (e.g., Kluth, 1986). This reactivation occurred along rift-initiated faults, which uplifted the Wichita and Amarillo regions and created the Anadarko Basin (Keller and Stephenson, 2007). During this same period, the Ouachita fold-thrust belt and the Arkoma foreland basin developed through continental collision (e.g., Elmore et al., 1990).

In the area of interest for this study (Figure 1b), the basement deepens to the west, from 610 m below sea level in the eastern portion of Osage County to more than 1525 m below sea level in the southwestern corner of Kay County (near the NFZ) (Crain and Chang, 2018).

### *Sedimentary cover*

In the area of interest of north-central Oklahoma, the crystalline basement is covered by a relatively thick layer of sedimentary units (Figure 1c). Our study focuses only on the lowermost section of the stratigraphy, primarily the Arbuckle Group. The Arbuckle Group is a sequence of predominantly limestone and dolomite, with minor shale and sandstone members (e.g., Johnson, 1996). This sedimentary succession is observed to be directly deposited on the unconformable basement surface; however, in some areas, the Arbuckle Group is separated from the basement by the Cambrian-age Reagan Formation, which was deposited in local depocenters (Elebiju et al., 2011). The Reagan Formation is either absent in the main study area (Osage County) or very thin (Carroll et al., 1999).

## Data and methods

### *3D seismic reflection data*

To assess the structure of the deep basement, we used eight 3D seismic reflection survey data sets. These surveys are in Osage and Kay counties covering an area of approximately 700 km$^2$, and they are sampled at 2 ms and poststack time migrated (Figure 1b, courtesy of Osage Nation and Spyglass LLC). The data were supplied in their interpreted and presented form as single stacks (the incidence angle ranges are unknown). The data were acquired and processed with the goal of imaging the sedimentary cover for hydrocarbon exploration. Therefore, imaging in the basement is relatively poor (average of 23 m in the sedimentary cover versus 30 m in the basement).

For brevity, of the eight surveys, we show maps and cross sections from three representative volumes (interpretation of all eight surveys is provided in the supplementary material), which include the Bois d'Arc, Wild Creek, and Big Heart surveys (Figure 1b). The three volumes are spatially distributed eastward from the NFZ, a structure that is of interest to our findings in this study. The Bois d'Arc survey is right at the western edge of the NFZ, the Wild Creek survey is approximately 40 km east, and the Big Heart survey is approximately 80 km east of the NFZ (Figure 1b). In the absence of well data, we constrain the identification of the top-basement and top-Arbuckle reflectors via a previous study that analyzed three of the same seismic volumes and tied the seismic volumes to well data (Elebiju et al., 2011). Because the goal was to study the structure near the top basement and intrabasement, we chose the z-crossing below both the top basement and top of the Arbuckle Group (Figure 2g–2i). A z-crossing is the point at which the instantaneous seismic amplitude has a value of zero when transitioning from a peak (local maximum) to a trough (local minimum).

For enhancement of the desired features on the top of the basement, three seismic attributes were selected. These attributes are the principal positive curvature, principal negative curvature, and energy ratio similarity. The intrabasement reflectors had only the energy ratio similarity applied. All of the attributes used were first computed volumetrically, then the instantaneous values were extracted onto the interpreted horizon.

Energy ratio similarity is a type of coherence attribute which highlights reflector discontinuity between seismic traces. This attribute has become widely used to identify and map geologic discontinuities of various types (Bahorich and Farmer, 1995). In this work, we select it for its ability to illuminate the reflector offset created by fault displacement. In general, the method is based on variations in the inline, crossline, and seismic amplitudes within a grid of traces (Bahorich and Farmer, 1995). Specifically, energy ratio similarity represents the ratio of the coherent and total energy within a given analysis window, where the total energy is the sum of the energy of each trace used to create the covariance matrix and the coherent energy is the sum of the energy of the principal component-filtered trace (Chopra and Marfurt, 2007). We computed the energy ratio similarity attribute using the AASPI software package. The algorithm uses a seismic amplitude volume and derived inline and crossline dip volumes. We chose to use a fixed rectangular analysis window with a window half-height of 10 ms. The spatial size of this window varies across the different data sets according to the inline and crossline spacing for a given survey (values are between 16.5 and 33.5 m for all volumes).

The two principal curvature attributes were computed to accentuate structures in the data because the purpose of this study was to analyze large-scale features in the basement of Oklahoma. This was done via AASPI using its dip-guided volumetric curvature algorithm. The inputs that go into this computation are an

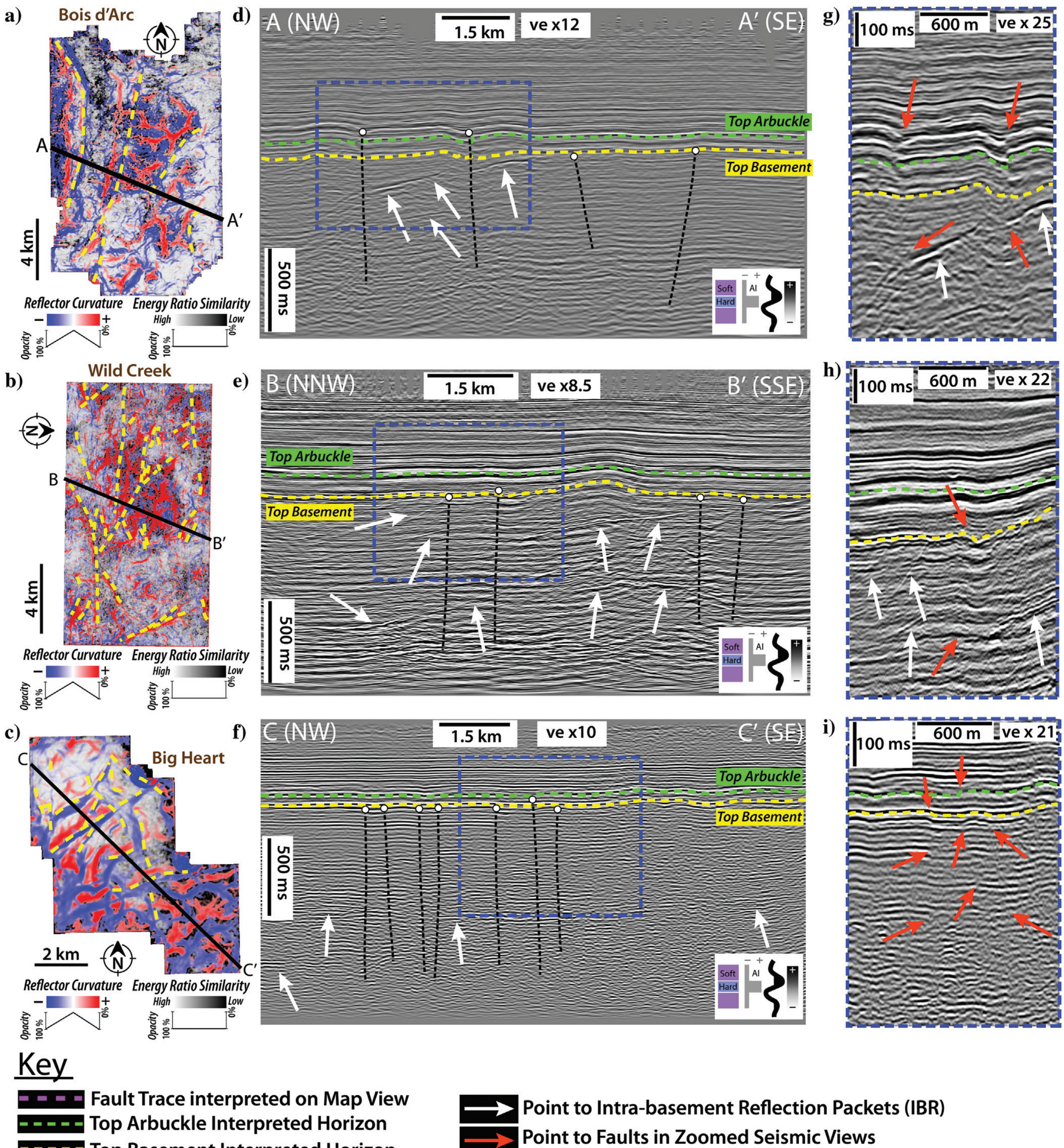


**Figure 2.** The intrabasement and through-going structures in the study area. For each survey, we show the (a–c) corendered energy ratio similarity and curvature (most-positive and most-negative) attributes extracted onto the top-basement surface and (d–f) 2D seismic cross section (vertical slice) overlaid with reflector and structural interpretations. The white circles on the fault traces represent the shallowest visible tip of the interpreted fault. (g–i) Magnified views of the seismic cross sections displayed in panels (d–f). The extent of these views is shown in panels (d–f) outlined by the blue dashed lines. On these magnified views, some of the faults that are interpreted on panels (d–f) are shown without the interpreted vertical trace. The red arrows point to the disruption that was used to validate the presence of the faults.

Downloaded 10/26/20 to 12.233.159.194. Redistribution subject to SEG license or copyright; see Terms of Use at https://library.seg.org/page/policies/terms
DOI:10.1190/INT-2020-0053.1

Downloaded 10/26/20 to 12.233.159.194. Redistribution subject to SEG license or copyright; see Terms of Use at https://library.seg.org/page/policies/terms
DOI:10.1190/INT-2020-0053.1

inline and crossline dip volume. From this, the software computes the optimized default parameters for the given volume. We chose a long wavelength calculation of the principal curvatures, which preferentially accentuates larger features. Computation is performed by defining a filter in terms of four wavenumbers $\lambda_1$, $\lambda_2$, $\lambda_3$, and $\lambda_4$ (all values are provided in the supplementary information). For the long-wavelength curvature, the wavenumbers are weighted as 1, 0.666, 0.333, and 0, respectively ($\lambda_4$ for all eight volumes that lie between 186 and 311 m). The filter then is convolved with the input data in the space domain (AASPI, 2019). The implementation of the positive and negative principal curvature is meant to highlight any curve that occurs in the seismic data between traces, the expression of which can represent a multitude of geologic features. Positive curvature highlights areas that have convex-upward structures (i.e., fault tip flexures, channel edges). Negative curvature reveals the locations of convex-downward features (i.e., channels, karsts) (Mai et al., 2014).

Following the interpretation, generation, and attribute extraction of key seismic surfaces, faults were interpreted. This interpretation was completed by observing lineaments of positive curvature, negative curvature, and/or energy ratio similarity on the generated horizon surfaces. Ideally, the fault character would be a low-similarity lineament flanked on one side by a positive-curvature lineament and on the other by a negative-curvature lineament. This signature would represent the fault's offset of traces (low similarity), the upthrown block (positive curvature), and the downthrown block (negative curvature) (Mai et al., 2014). However, it is possible for faults to be expressed by only one of these features. So, these signatures were identified in map view and verified in profile view. Arbitrary seismic profiles were created for each fault analyzed. The trend of the arbitrary section was set to be generally perpendicular to that of the fault. In cases in which faults possess considerable deviation in trace strike, multiple profile orientations were generated. Although the imaging was relatively poor in the basement, we attempted to observe the consistent offset of small reflector packages in the basement or in linear/planar zones of consistent disruption. In many cases, the geometry of faults within the basement could not be fully and confidently outlined. However, the expression of the attributes at the top basement strongly suggests the presence of a fault (Figure 2).

After the fault presence was established for all attribute-enhanced lineaments, their degree of upward continuation was examined. For this analysis, the goal was to determine the vertical extent of each fault segment. To accomplish this, the identified fault traces at the top of the basement were displayed in 3D space again using the arbitrary cross sections. Each arbitrary cross section was displayed and brought to one end of the fault. The cross section was then scrolled along the length of the fault. At each step, the cross section was examined, focusing first on the top basement reflector to find the location of the previously identified basement-penetrating fault. Then, the seismic units above the basement fault location were examined, looking for the continuation of the fault up section (the reflector offset). This was completed first within the Arbuckle Group interval and then above the Arbuckle Group interval. These data then were recorded as two groups: the faults that showed displacement of seismic reflectors at the top-basement horizon and within the Arbuckle Group and the faults that showed displacement above the top of the Arbuckle Group reflector. In effect, this analysis created three discrete groups of faults: (1) faults that show displacement only within the basement; (2) faults that have displacement in the basement and into the Arbuckle Group; and (3) faults that cut through the basement, through the Arbuckle Group, and into the sedimentary lithologies above the Arbuckle Group.

### *Quantitative fault analysis*

To assess the spatial variability of the analyzed faults, two calculations were performed using the collected fault trends and lengths. The first is the fault areal density. The fault areal density was calculated by dividing the number of faults in each 3D volume by the area of that survey. This results in a single value for each survey in units of $\mathrm{km}^{-2}$. The second calculation performed with the collected fault data was to determine the fault areal intensity. This was performed by first summing the length of all of the faults within a given survey. The value then was divided by the area of the survey, resulting in a single value per survey in units of $\mathrm{km}^{-1}$.

Finally, the vertical separation for all of the faults was measured. Vertical separation is a measure of the across-fault offset for ductile and brittle fault-associated deformation. It is akin to vertical throw, although not as strictly defined. The measurement of vertical separation was done using the previously described fault-perpendicular arbitrary cross sections. Each cross section was displayed at one end of the fault trace and the fault's position at the top of the basement was located. The section then was sequentially scrolled at spatial steps of approximately 330 m. The offset was measured at the top of the basement. This was compared to the up-thrown and down-thrown elevations of the deformed basement surface. Because the data are in the time domain, these values were recorded in two-way traveltime (TWT) milliseconds.

## Results

### *Basement deformation*

#### *Intrabasement reflection packets*

Present in the basement are distinct packets of coherent, laterally continuous, relatively higher amplitude reflectors (intrabasement reflectors [IBRs]; Figure 2d–2i), which commonly show shallow dipping geometries and cross-cutting relationships, and they often bifurcate into multiple segments. Although we observe these features in all eight seismic surveys, they vary in aerial

Downloaded 10/26/20 to 12.233.159.194. Redistribution subject to SEG license or copyright; see Terms of Use at https://library.seg.org/page/policies/terms
DOI:10.1190/INT-2020-0053.1

extent and magnitude of segmentation. The mapped IBRs show varying dip directions, which include north (e.g., Figure 3a), west (e.g., Figure 3b), and south (e.g., Figure 3c). The lineaments of the low-energy-ratio similarity attribute along the mapped IBR surfaces delineate discontinuity planes that exhibit mean trends along the northeast–southwest to east-northeast–west-northwest (e.g., Figure 3a and 3c) and north-northwest–south-southeast (e.g., Figure 3b).

*Top-basement structure*

The basement is seismically identified using two main criteria. First, the crystalline basement has a distinctive seismic character from the sedimentary cover. It presents a low-amplitude, discontinuous, chaotic, highly variable reflectivity (Figure 2d–2f), which likely is controlled by the lack of bedding and comparatively high homogeneity in igneous rocks (few high-impedance contrasts). Second, the top-basement reflector itself is characterized by a relatively high negative amplitude and generally is continuous throughout the seismic volume (Figure 2). By contrast, the intrabasement reflectors in the seismic volumes typically are discontinuous, high-amplitude, and a strong trough-peak or trough-peak-trough reflector packet (Figure 2). Like the top-basement reflector, the most continuous of the intrabasement reflectors were fully picked when possible.

As mentioned previously, three representative volumes have been selected for display in this manuscript: the Bois d'Arc, Wild Creek, and Big Heart (Figures 1b, 2, and 4). When examining the picked surfaces in TWT (Figure 4), structures begin to emerge. Figure 4a shows a surface that dips to the southwest and has a scattering of localized highs near the center of the survey. Figure 4b shows a surface that dips to the southwest and shows a few lineaments that generally trend northeast–southwest. Similarly, the surface in Figure 4c shows a surface that dips toward the southwest and shows lineaments trending northeast–southwest. All dips observed generally agree with the regional dips put forth by Crain and Chang (2018) (see the supplementary figures).

There are six key features that can be observed on each TWT basement surface. These features include visible fault traces, structural highs, ring-shaped structural highs, linear structural highs, linear structural lows, and broad structural lows (Figure 4). The Bois d'Arc surface is dominated by a large (4 km diameter) ring-shaped structural high (66 ms or approximately 200 m) surrounded by multiple linear structural highs. Near the western edge of the survey, there are coupled linear positive and linear negative flexures that strike north–south (Figure 4a). The Wild Creek surface possesses a very broad structural low to the west with multiple closely spaced structural highs in the east, and numerous linear highs and linear lows are interspersed (Figure 4b). The top-basement surface from the Big Heart survey reveals comparable structures, with two closely spaced structural highs in the southeast corner and two similarly spaced broad structural lows just to the northwest. Also present are numerous visible fault traces that trend predominantly northeast–southwest (Figure 4c).

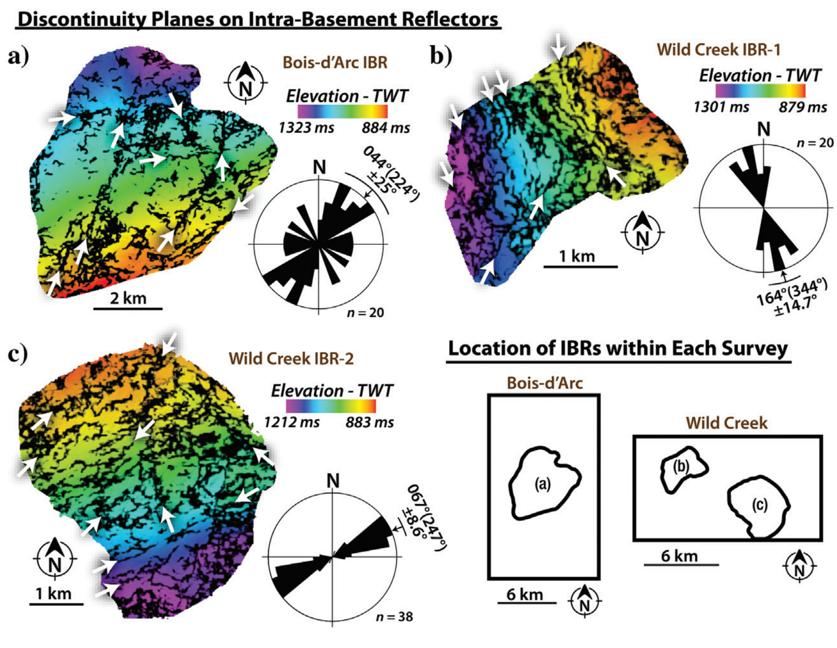


**Figure 3.** Trends of potential fault traces at depth in the basement. Corendered time-depth and energy-ratio similarity attributes on surface maps of the largest IBRs mapped in the (a) Bois d'Arc and (b–c) Wild Creek surveys. The white arrows point at lineaments of low-energy-ratio similarity (i.e., discontinuity lineaments). The rose diagrams show the frequency-azimuth distribution of the lineaments. The location of the intrabasement surfaces within their given survey are shown in the diagram in the lower right.

When attributes are extracted, the orientation of the lineaments at the top of the basement becomes clearer. In general, most lineaments correspond to high values of negative curvature (Figure 2a–2c). In many cases, these trends are accompanied by a corresponding positive curvature lineament, and, for even fewer, a low-energy-ratio similarity zone can be observed between the two (Figure 2). Also seen at the top of the basement are large regions of high positive curvature (Figure 2a–2c). These typically are circular and elliptical in shape (in map view) and commonly are bounded by low-curvature regions (Figure 2a–2c). Looking at the interpreted top-basement horizons with extracted attributes from the three representative volumes, there is a change in the dominant trend of the lineaments (Figure 2a–2c). These trends rotate from approximately north–south in the west (Figure 2a) to progressively northeast–southwest and west-northwest–east-southeast in the east (Figure 2b and 2c). In the seismic cross section, the interpreted basement faults appear as discontinuities of the top-basement reflector packet or areas of dimmed or disrupted amplitude that cut down into the basement. Disruption in the basement often is poorly imaged and characterized by consistent low-amplitude zones. However, many faults can be seen intersecting intrabasement reflectors. Typically, the observed faults dip vertically to subvertically in TWT.

### *Top-Arbuckle structure*

The Arbuckle Group's seismic expression is defined by a high-amplitude peak-trough packet that generally is continuous. Internally, reflectors generally are low-amplitude, parallel, and discontinuous. Similar features to those observed at the top-basement surface are seen on the top-Arbuckle TWT surface. In the Bois d'Arc surface, there is a large ring-shaped structural high in the north-central region. Surrounding this are numerous linear structural-high and fault traces. In the western part of the survey, there is a pair of directly adjacent linear low and linear high (Figure 5a). In the Wild Creek survey, there are four large structural highs in the east and a broad structural high in the west. Also observed in the west are a linear structural low and a linear structural high (Figure 5b). The top-Arbuckle surface for the Big Heart survey reveals a large structural high in the southwest corner that is flanked by a broad structural low to the south. Near the east-central region, there is a cluster of features. There are multiple visible fault traces that separate a linear structural high and a linear structural low. Also observed in this area are two broad structural lows.

### *Azimuthal distribution of the mapped faults*

With all the faults interpreted at the top-basement horizon, the azimuths were combined to show the overall observed fault trends. The result of this compilation can be seen in the rose diagram (Figure 6), which re-

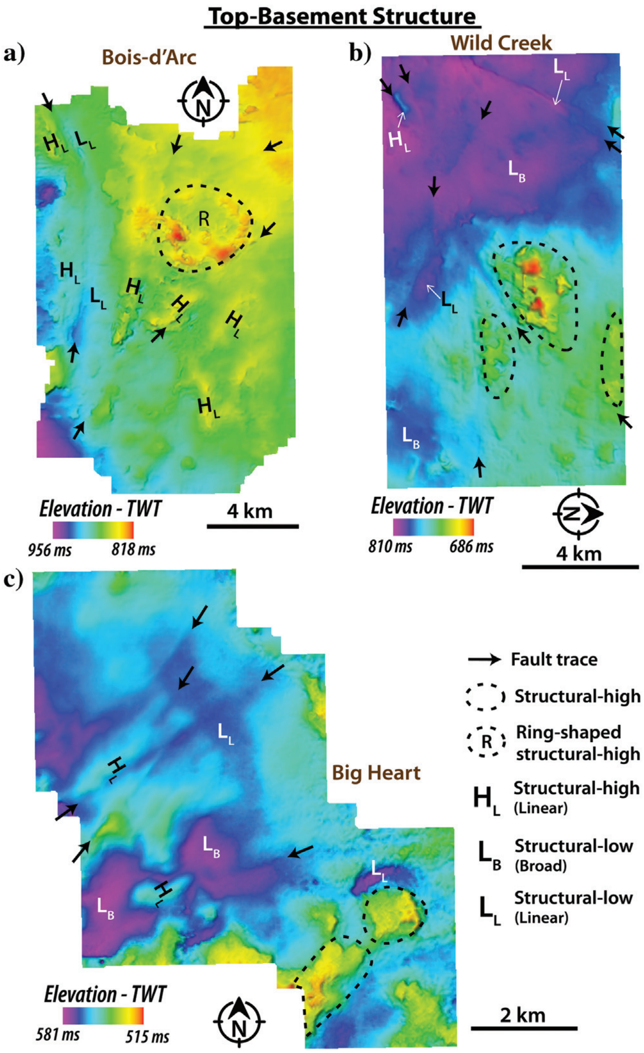


**Figure 4.** Representative top-basement structures: (a) Bois d'Arc, (b) Wild Creek, and (c) Big Heart. The surfaces show examples of the common top-basement structural features observed in all of the surveys.

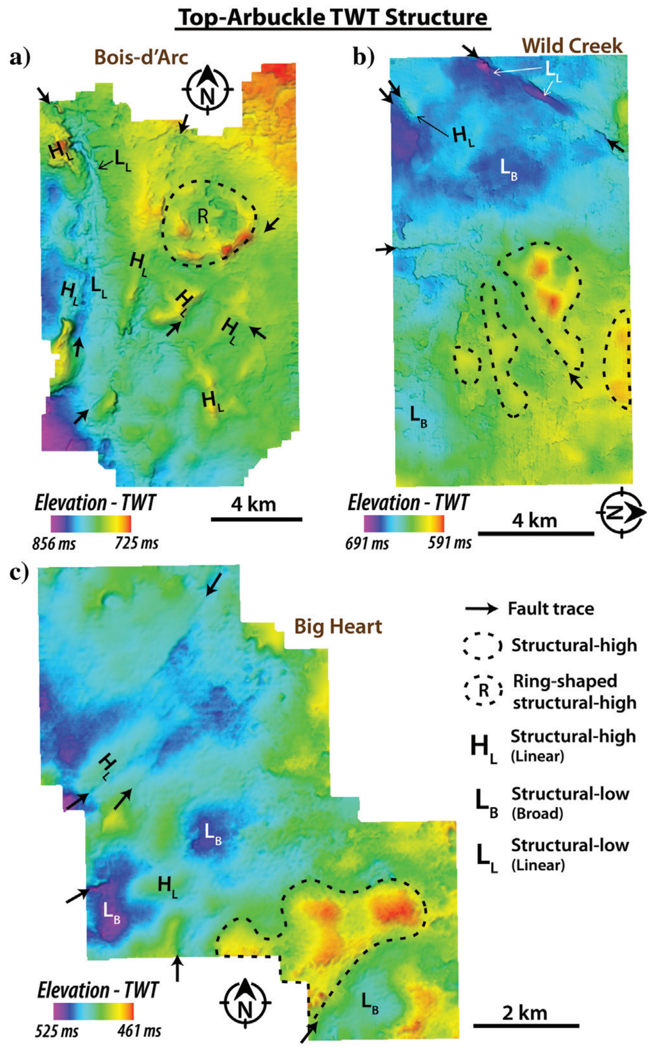


**Figure 5.** Representative top-Arbuckle structures: (a) Bois d'Arc, (b) Wild Creek, and (c) Big Heart. The surfaces show examples of the common top-Arbuckle structural features observed in all of the 3D seismic surveys.



Downloaded 10/26/20 to 12.233.159.194. Redistribution subject to SEG license or copyright; see Terms of Use at https://library.seg.org/page/policies/terms
DOI:10.1190/INT-2020-0053.1

veals three main clusters of fault trends, north–south, northeast–southwest, and west-northwest–east-southeast. These reported azimuthal frequency groups were selected based on breaks in the data. These breaks are locations where there is a drop in the overall frequency of a group of the azimuthal frequency data. These are observed at 165°/345° and 020°/200°, which creates the north–south trend, 165°/345° and 080°/260° delineating the west-northwest–east-southeast trend, 020°/200° and 080°/260° which demarcates the northeast–southwest trend. Of these, the northeast–southwest group is the most numerous. Based on this separation, the three groups have calculated means of 005°±8.2, 056°±10.2, and 103°±9.3, respectively (Figure 6). These generally agree with trends observed in a study of Oklahoma fault and fracture trends using numerous methods (Kolawole et al., 2019).

With the broader trends identified for the region, a closer look was taken at the individual surveys. The survey area and the total number of faults within the given survey were used to determine the fault areal density and fault areal intensity. First, the two measured values were plotted with distance from the Bois d'Arc survey (Figure 7c). The survey areas that were examined have area ranges from near 200 $km^2$ to under 100 $km^2$. The total number of faults for the surveys varies drastically, although the fault number generally increases from the east, with 6 faults in the Bois d'Arc survey to the west, with 17 faults in the Big Heart survey. The fault areal density shows a consistent increase with distance from the Bois d'Arc survey. Values begin at near-zero $km^{-2}$ in the Bois d'Arc survey and ends at the Big Heart survey with a density of 0.23 $km^{-2}$. Similarly, the areal fault intensity increases with eastward distance. In both cases, there is a peak at the Wild Creek survey meaning there is an anomalous number and length of faults compared to its survey area.

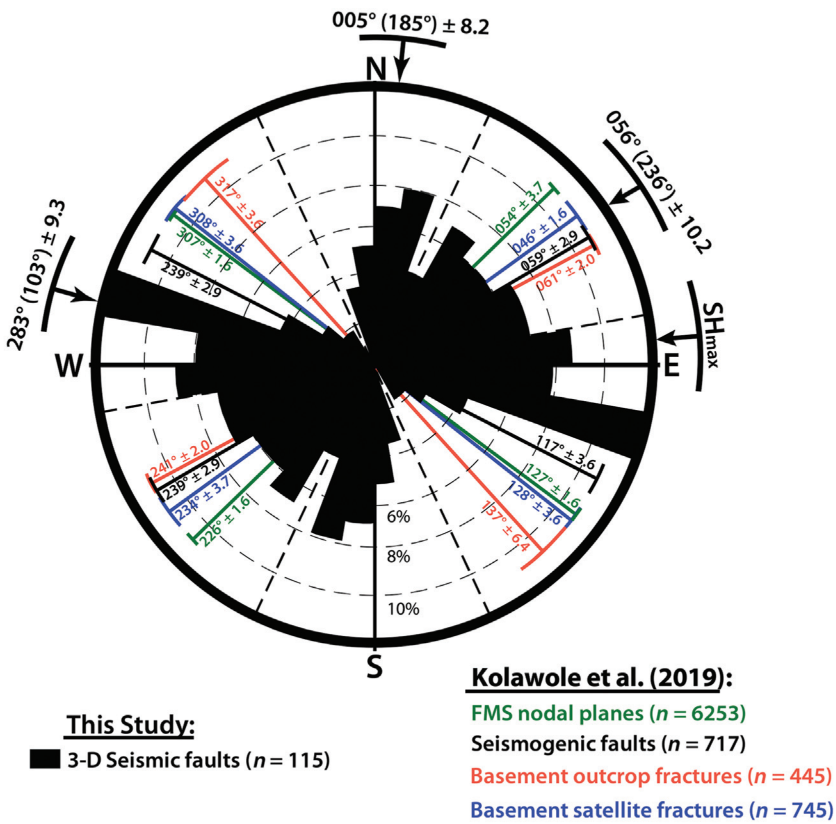


**Figure 6.** Comparison of 3D seismic fault trends with the regional basement fabric. Rose diagram of fault strikes mapped from the top-basement surface of the eight seismic data sets overlaid on a rose diagram of mean trends of basement faults mapped from various independent methods (trends modified after Kolawole et al., 2019). Structural trends are described as mean trend (= mean trend + 180°). The gray dotted lines are the dividing lines for the 3D seismic fault prominent trends, and $S_{Hmax}$ represents the present-day regional maximum horizontal compressional stress direction (from Alt and Zoback, 2017; Qin et al., 2019). The plots show that the regional northeast–southwest- and northwest–southeast-dominant trends align well with the northeast and west-northwest–east-southeast mean trends in the 3D seismic faults.

### Spatial distribution of vertical separation

The maximum vertical separation point was determined from the compiled data for each of the 115 faults in the study. These data were grouped by survey, and the largest maximum vertical separation observed at the top-basement horizon in the volume was selected. This was then plotted in terms of maximum vertical separation versus eastward distance from the western edge of the Bois d'Arc survey (Figure 7d). Values of vertical separation range between 20 and 50 ms or 60 and 150 m (given a constant basement velocity of 6000 m/s; Kibikas et al., 2019). When plotted spatially, the maximum vertical separation for each survey shows a negative correlation with eastward distance (Figure 7d). In other words, the largest vertical offset is found in the westernmost survey, the Bois d'Arc (Figure 7), and tends to decrease eastward. There is a slight discrepancy with the values for the easternmost surveys. The faults found in the Gray Horse survey possess slightly lower values than expected by the line of best fit whereas the Antelope and Pearsonia vertical offset values are higher than would be predicted. However, these still follow the trend because their quantities are predominantly less than the separation values found in the surveys to the west (Figure 7c).

### Proportions of propagated basement deformation into the post-Arbuckle sequences

To assess the structural connectivity of the basement and sedimentary cover via through-going faults, the basement-



Downloaded 10/26/20 to 12.233.159.194. Redistribution subject to SEG license or copyright; see Terms of Use at https://library.seg.org/page/policies/terms
DOI:10.1190/INT-2020-0053.1

rooted structures were examined to assess their level of upward continuation. Several of the 115 identified faults are observed to be directly cutting the sedimentary cover, with additional evidence of basement highs and fault-related deformation having deformed the overlying sedimentary strata (Figure 2). Specifically, 32 basement-rooting faults clearly cut into the Arbuckle Group directly overlying the basement. Of these 32, there are 26 faults that extend above the Arbuckle Group. Therefore, approximately 28% of the faults identified terminate within the Arbuckle and approximately 23% continue upward into post-Arbuckle sedimentary units. Spatially, the proportion of faults that cut into the sedimentary cover decreases eastward with distance (Figure 7d). The number of faults that terminate in the post-Arbuckle units is highest in the west and smaller in the east. Near the center of the data region, there are no faults that are observed that extend above the Arbuckle Group (Figure 7d).

## Discussion

### Basement deformation in north-central Oklahoma

#### Basement-bounded igneous intrusions

The pervasive, intrabasement reflectors observed in the study area previously have been interpreted to be either basement fault damage zones (Liner, 2015) or igneous sheet intrusions (Elebiju et al., 2011, Kolawole et al., 2020). The fault damage zone interpretation lacked supporting independent data and primarily is amplitude based. The intrabasement reflectors show a trough-peak-trough, also observed in the data sets analyzed in this study (e.g., Figure 2a and 2b). Using the American convention for polarity, this wave train would represent a boundary across which impedance decreases (i.e., the negative RC boundary). However, without proper knowledge of the phase characteristics with depth, strong side-lobe effects, etc. in the seismic data, such an interpretation of IBRs may be erroneous. The IBRs observed in this study are similar to those observed elsewhere in the granitic basement of the U.S. Midcontinent and are interpreted to be composed of mafic materials associated with the Precambrian Midcontinent Rift (Hinze et al., 1997). The structure and distribution of the IBRs, which include shallow dips, segmentation, limited spatial extents, and common cross-cutting geometries, are consistent with IBRs observed in some other geologic settings (e.g., Cartwright and Hansen, 2006, Magee et al., 2016).

To better understand the composition of the IBRs, we consider observations in the basement-penetration well data within the study area (approximately 1.2 km basement-penetration Wah-Zha-Zhi well, Osage County,

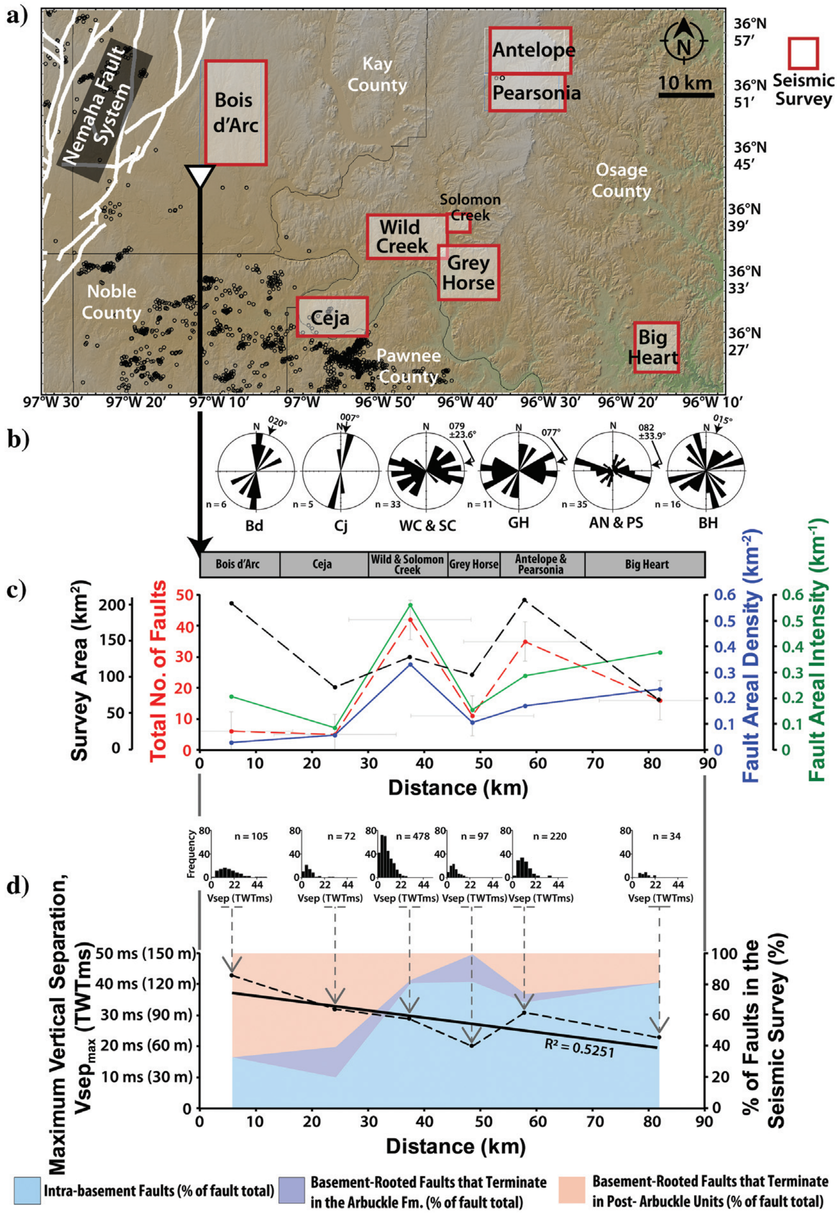


**Figure 7.** Spatial distribution of the deformation intensity with respect to the location of the NFZ: (a) map of the study area showing the locations of the seismic surveys used in this study. The black circles are the 2010–2017 earthquakes (source: Oklahoma Geological Survey Catalog). (b) Rose diagrams showing the frequency-azimuth distribution of the mapped faults in each survey (AN, Antelope; Bd, Bois d'Arc; Cj, Ceja; BH, Big Heart; GH, Gray Horse; PS, Pearsonia; and WC, Wild Creek). (c) West to east spatial distribution of the total number of mapped faults in each survey, the size of the interpreted surveys, and the fault areal density and intensity. (d) West to east spatial distribution of fault-related vertical separation (Vsep) measured along the mapped basement-rooting faults in each seismic survey. The histogram represents the overall statistics of the measurements, and the main plot shows the trend of the maximum Vsep measured in the seismic data.



Downloaded 10/26/20 to 12.233.159.194. Redistribution subject to SEG license or copyright; see Terms of Use at https://library.seg.org/page/policies/terms
DOI:10.1190/INT-2020-0053.1

Downloaded 10/26/20 to 12.233.159.194. Redistribution subject to SEG license or copyright; see Terms of Use at https://library.seg.org/page/policies/terms
DOI:10.1190/INT-2020-0053.1

Chopra et al., 2018) and southwest of the study area (120 m basement-penetration KF2 well, Kingfisher County, Kolawole et al., 2020). The Osage County basement cuttings showed granite, rhyolite, and gabbro chips; more compellingly, the Kingfisher County basement cuttings and wireline logs show alternation of granite and gabbro/diabase rocks. Analysis of the seismic reflection signature and forward modeling of the well log data of the Kingfisher County basement units suggest that the IBRs are, in fact, mafic igneous sill intrusions in the basement of Oklahoma (Kolawole et al., 2020).

Furthermore, the pervasive discontinuity lineaments that cut the IBR surfaces (Figure 3) provide additional insight into the nature of the basement deformation. The trends show low-energy-ratio similarity signatures and commonly offset the IBR packets by a small amount. These characteristics also were observed in the Kingfisher County basement and have been interpreted as intrabasement faults, among which some may have been reactivated and propagated up into the sedimentary cover sometime after the emplacement of the sills (Kolawole et al., 2020).

*Basement faulting and deformation of the basement surface*

A study by Guo and George (1999) analyzed faulting across the midcontinent (e.g., Oklahoma, Kansas, Nebraska, and Iowa). The authors found that there are three predominant fault trends across the midcontinent: northeast–southwest, west-northwest–east-southeast, and a minor trend north–south that is controlled by the NFZ. This previous observation supports our observations of a minor trend following 005° and two major trends along 056° and 283° (Figure 6). The study conducted by Guo and George (1999) also found similar dominant faults and fracture trends that appear in overlying sediments and at the surface. Based on this observation, the authors concluded that there have been multiple stages of reactivation, which have facilitated propagation to the surface. We do not observe any evidence of faults propagating to the surface. Schwab et al. (2017) examine a seismic survey in south-central Kansas and found similar features to those shown here (basement highs and fault traces at the top basement surface). They interpret a single 3D seismic reflection volume, find deep faults, and assess the seismic hazard. In total, they find 12 steeply dipping faults, of which 3 cut down into the basement. Their trends of north and north–northeast are consistent with our observations in north-central Oklahoma.

Further research conducted by Kolawole et al. (2019) examines multiple data types to identify preexisting faults and fractures in Oklahoma's Precambrian basement. The authors combine multiple methods of fault and fracture identification to clearly and definitively define the nature of the existing basement structure. These include faults identified by relocated earthquake data, fractures identified in outcrop, fractures identified from satellite images, and nodal planes from focal mechanism solutions. The results from their analysis show predominant trends of faults and fractures in the northeast–southwest and west-northwest–east-southeast directions. These resultant trends match two of those presented in this work, with the west-northwest–east-southeast trend being the worse of the two fits. In the results of Kolawole et al. (2019), the most westward trend is 297°, whereas in this work, the mean azimuthal direction for this general west-northwest–east-southeast trend is 283° ±9.3 (Figure 5). This discrepancy is relatively minor and still supports the assertion that a predominant trend of faults and fractures exists in the Precambrian basement. The other trend (northeast–southwest) shows excellent agreement with the prior work (Figure 5). The mean trend of 056° falls directly within the grouping of those shown in Kolawole et al. (2019).

There have been two other geophysical studies that focused on the basement structure in Osage County, Oklahoma. Elebiju et al. (2011) consider seismic and aeromagnetic data for fault interpretation, and they find that in the region, faults had a clearly dominant northeast–southwest trend for subsurface structures. Our results, however, do not show the same dominance of the northeast–southwest trend. Instead, the northeast–southwest and west-northwest–east-southeast trends appear somewhat similar in frequency to one another with the west-northwest–east-southeast trend being slightly more dominant (Figure 6). A possible explanation for this lies in seismic coverage and resolution. In terms of coverage, the surveys are limited spatially. As previously mentioned, the resolution of these seismic volumes is quite poor at depth (approximately 30 m). The faults interpreted in the study generally are relatively large in spatial extent, with the smallest being approximately 0.5 km long. Therefore, if there are many small west-northwest–east-southeast-striking faults, it is unlikely that they would be captured in our interpretation. We do, however, see an instance of fault intersection like that in Mai et al. (2014) within the Big Heart survey (Figure 2c). On the top of the basement, numerous northeast–southwest-striking faults appear to be disrupted by a pair of west-northwest–east-southeast faults (Figure 2c). This is supported by the observations made in Mai et al. (2014). Here, they see a common occurrence of close to east–west faults within the same region of investigation.

Based on prior work that defined the geometry of the Midcontinent Rift in Oklahoma (Stein et al., 2014), there is the potential that an interpreted gravity anomaly in northern Oklahoma constitutes a rift jump segment (as defined by Nelson et al., 1992). Our study area is located directly to the east of the interpreted Midcontinent Rift in Oklahoma. The proximity to the rift makes it likely that the deformation described in this paper is in some way related to the opening of the rift. This is most clearly shown in the rotation of the fault trends with distance from the NFZ. Based on the observed faulting patterns, two plausible hypotheses exist. The faulting pattern

Downloaded 10/26/20 to 12.233.159.194. Redistribution subject to SEG license or copyright; see Terms of Use at https://library.seg.org/page/policies/terms
DOI:10.1190/INT-2020-0053.1

could suggest distinct periods of rift-perpendicular and rift-oblique opening. It also could be the case that the northeast–southwest and west-northwest–east-southeast trends are faults associated with the more dominant (longer) north–south-striking faults. Due to the supposed time period of opening (Figure 1c), we believe the latter is more plausible.

A more recent study (Kolawole et al., 2020) studied a similar area through comparable methods and found results that coincide with those provided in this work. The authors used a newer 3D seismic data set to discern the structure of the basement in Kingfisher County, Oklahoma. They showed that there are clear, steeply dipping, basement-rooted faults that cut upward into the sedimentary cover. Although the study is limited to a single survey, they also observe trends similar to those reported here. Three large basement-rooted faults are observed within the 3D seismic volume. The faults that are observed either cut upward and through a portion of the sedimentary cover or generate monoclinal flexure. This is comparable to the results shown in this paper with a portion of the faults showing offset in the sedimentary cover and the remainder creating folds in the units above the basement.

The quantification of maximum vertical offset for the interpreted faults reveals a compelling trend. The fewest faults were observed and mapped in the survey most proximal to the NFZ (Bois d'Arc Survey), and the trends show an eastward increase in the fault density and intensity, with an associated decrease in the maximum vertical separation. This suggests that proximal to the NFZ, most of the deformation is accommodated along few fault segments; however, in the far-field from the Nemaha domain, deformation may be accommodated by distributed and relatively shorter fault segments (diffused strain).

### *Deformation of sedimentary sequences, structural styles, and spatial distribution of inherited strain*

There are clear structural similarities between the structure of the top-basement and top-Arbuckle TWT surfaces extracted from all of the 3D surveys, showed in the case of the Bois d'Arc survey, a large, ring-shaped structural-high is clearly visible to the north. Similarly, linear basement structural highs appear on the overlying Arbuckle surface. These observations and similar seen in other surveys show a link between the basement structures and the overlying structures in the Arbuckle Group.

The proportion of basement-rooted faults that do not penetrate the cover increases eastward away from the NFZ. Additionally, the relative proportion of faults that penetrate formations shallower than the Arbuckle Group decrease away from the NFZ (Figure 7d). Faults that terminate within the Arbuckle Group occur mostly at an intermediate distance. We conclude that during the Alleghenian Orogeny, which affected the region, basement-rooted faults primarily were reactivated near the NFZ. This is perhaps why we observe more reactivated faults of which none tipped out within the Arbuckle Group.

In the sedimentary cover, the structural link to the basement is manifested in a multitude of ways, which are expressed mainly in four simple structures: monoclinal flexure, pop-up features, negative flower struc-

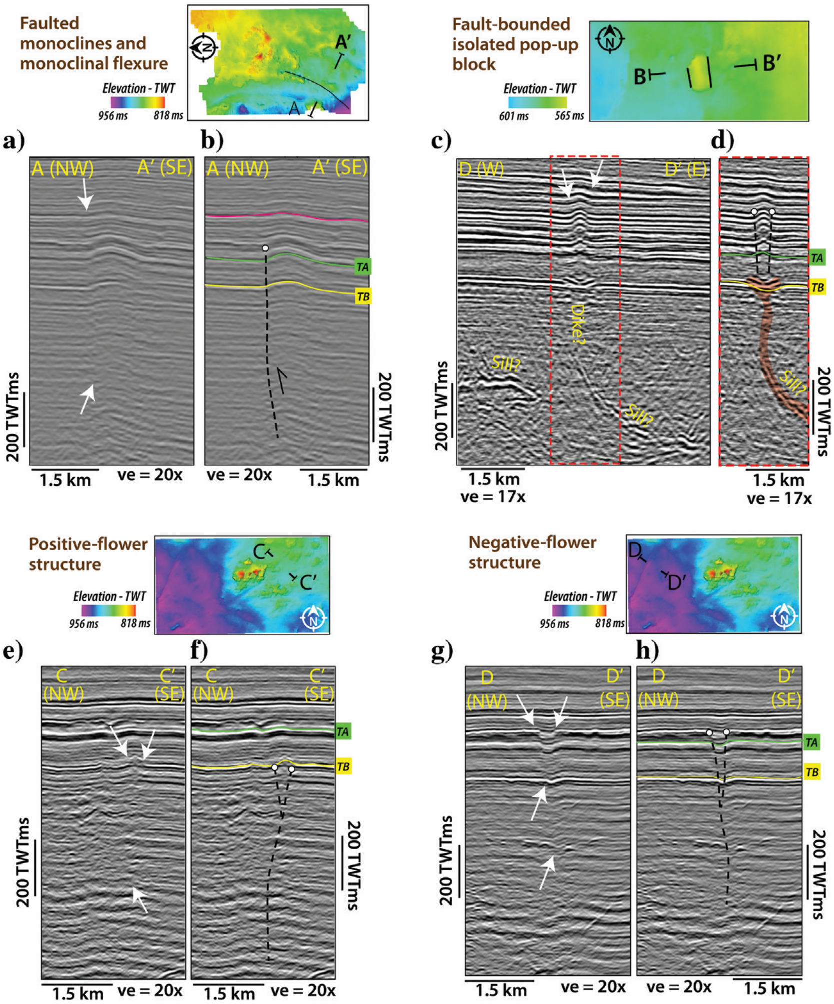


**Figure 8.** Structural styles of basement-rooted faults in the study area: (a and b) faulted monocline and monoclinal flexure (representative example from the Bois d'Arc survey), (c and d) fault-bounded isolated pop-up block (representative example from the Gray Horse survey), (e and f) positive-flower structure (representative example from the Wild Creek survey), and (g and h) negative-flower structure (representative example from the Wild Creek survey). For each cross section, the location of the line is shown in map view above.

Downloaded 10/26/20 to 12.233.159.194. Redistribution subject to SEG license or copyright; see Terms of Use at https://library.seg.org/page/policies/terms
DOI:10.1190/INT-2020-0053.1

tures, and positive flower structures. The most common of these is the monoclinal flexure of the sedimentary cover (Figure 8a and 8b). The two possibilities for the formation of these features are passive and active deformation. In the active case, the preexisting basement fault propagates into the sedimentary cover following deposition (possibly subseismically). In the passive case, the folding mechanism occurs as the unit is deposited, through differential compaction. The second commonly observed feature is an isolated pop-up feature found in the Gray Horse survey (Figure 8b). In this case, there is a small, elliptical feature with a high amplitude to wavelength ratio that is observed in the sedimentary cover. The feature propagates high into the sedimentary cover and overlies a saucer-shaped feature at the top of the basement (Figure 8c and 8d) Although the geometry of the feature is somewhat confounding due to its symmetry and amplitude, it coincides with the location of a basement sill that appears to turn sharply upward. A possibility for the cause of this feature is forced folding above a top-basement intrusion. The final two examples are interpreted positive and negative flower structures from the Wild Creek survey. The positive structure shows two steeply dipping faults that appear to converge in the deep basement (Figure 8e and 8f). Similarly, the negative flower structure has a steeply dipping basement fault that appears to branch near the top of the basement (Figure 8g and 8h). These structures suggest the presence of strike-slip motion along their respective faults. Although the exact timing cannot be determined, few features cut above the Arbuckle Group. This suggests that this regime was present in the early Phanerozoic or the stress field that generated these features was not sufficient to propagate faults significantly up section within this study area. The second of these is the more likely due to the previously established Alleghenian Orogeny that occurred during the Carboniferous, inverted the SOA, and created the Nemaha uplift.

### *Implications for seismicity in Northern Oklahoma*

Oklahoma sits near the center of an amalgamated continental plate at considerable distance from any active plate boundary and thus experiences only far-field stresses. However, these stresses still are sufficient to produce natural tectonically driven earthquakes within the state. These have been recorded for decades showing an average of M > 3 21 events per year (Ellsworth, 2013). There also is the potential for larger magnitude natural seismicity, as evidenced by the recent (Holocene) paleoseismic record of the Meers Fault (Crone and Luza, 1990) and the 1952 Mb = 5.5 El Reno earthquake (Luza and Lawson, 1983). However, these events occur with relatively low frequency. Starting in late 2009, Oklahoma experienced a phenomenal increase in the number of earthquakes (Ellsworth et al., 2015). This growth continued for years, eventually placing Oklahoma at the same level as California and Alaska for the most seismically active U.S. states. Although the precise mechanisms for increased seismicity is under debate, previous studies have shown a direct correlation between the large volumes of subsurface wastewater injection and the spike in seismicity (e.g., Keranen et al., 2014; Ellsworth et al., 2015). In conjunction with this, it has been shown that many of the earthquake sequences during this period have occurred on previously unmapped faults (Walsh and Zoback, 2016; Kolawole et al., 2019). A prominent example is the 2016 Mw-5.8 Pawnee, Oklahoma event which ruptured an unknown fault between the Stillwater and Labette faults (Barbour et al., 2017). Although produced water is dominantly disposed of in the Arbuckle Group, the earthquakes clearly are not occurring in this interval. Rather, these events occur at depths between 2 and 8 km below sea level with a mean of approximately 6.5 km (Schoenball and Ellsworth, 2017), placing the events fully within the Precambrian basement in most of north-central Oklahoma.

Through attribute enhancement of seismic data, this study identified 115 faults expressed at the top and downward cutting into the basement. Whereas some of these faults appear in the Oklahoma fault catalog (most notably the Labette fault and a large NFZ segment near Peckham, OK) the vast majority had not been previously identified. The primary implication of these conclusions is on earthquake hazard within the state, as induced seismicity is occurring on unknown faults. The known $SH_{max}$ orientation in Oklahoma is 085° ± 005° (Alt and Zoback, 2017), which results in a range of optimal orientations for fault failure of 40°–60° and 130°–150° in the current stress regime (Holland, 2013). Using these orientations, the data shown in Figure 6 were examined. All faults within these two 20° azimuthal ranges of fault failure were summed. The result was that 16.5% of the 115 faults compiled in the study fall within the optimal range for failure. Although this is true in a general sense, it does not consider some intricacies such as local stress rotation or fault history (stage in recurrence). However, it must be noted that although the main area of study (Osage and Kay Counties) has experienced some natural seismicity in the past (Luza, 2008), it has not experienced significant induced seismicity relative to the surrounding counties.

Another facet of the fault interpretation was to analyze the number of faults that cut above the basement and above the Arbuckle Group. We found that approximately 28% of the 115 faults cut into the Arbuckle Group and approximately 23% cut into the sedimentary formations above it. It is possible that a purely poroelastic response could trigger far-field basement-hosted seismicity due to fluid injection in an overlying sedimentary unit (Segall and Lu, 2015). However, there is the potential for a directed pore-pressurization earthquake triggering due to proximity to a basement-rooted fault (Segall and Lu, 2015). There also is the potential for a direct injection-induced reactivation of basement faults via fluid pathways (i.e., secondary interconnecting faults and fractures). Direct fluid conduction could increase the pore pressure around a fault or in the long term alter fault core chemistry and thus fault strength and slip po-

Downloaded 10/26/20 to 12.233.159.194. Redistribution subject to SEG license or copyright; see Terms of Use at https://library.seg.org/page/policies/terms
DOI:10.1190/INT-2020-0053.1

tential. The faults that we identify show that brittle deformation is not confined to the basement and suggests that the through-going fractures represent fluid migration pathways that link the relatively shallow sedimentary units to the basement. Additionally, the spatial distribution shows that there is a stronger coupling of basement-sedimentary faulting in areas that are in the proximity of the NFZ than at distal areas (Figure 7d). Thus, there may be a higher seismic hazard related to sedimentary fluid injection in areas proximal to the NFZ.

## Conclusion

Our analyses revealed 115 basement-rooted faults that show dominant trends of west-northwest–east-southeast, northeast–southwest, and north–south. The prominent west-northwest and northeast trends of the faults coincide markedly with the trends of the recent seismicity lineaments in the region. In addition to basement faulting, we also observed the presence of several intrabasement reflection packets, interpreted as Precambrian mafic sills, which represent an additional component of basement deformation in north-central Oklahoma. The intrabasement reflectors can be observed in all eight of the analyzed seismic data sets; however, they are more pervasive in some and less in others. Proximal to the NFZ, the north–south fault trend appears to dominate, but it transitions into northeast–southwest and west-northwest–east-southeast further east.

Results on the first-order spatial distribution of vertical separation suggest that proximal to the NFZ, deformation is dominantly accommodated along a few elongate fault segments, and farther away, the deformation is distributed across shorter fault segments. Additionally, the shallow reaches of the fault segments suggest the potential for spatially pervasive fluid conduction.

Furthermore, 16.5% of the mapped faults fall within the range of optimally oriented faults within Oklahoma given the present-day stress field $SH_{max}$ = 085°. Additionally, of the 115 faults that were identified, approximately 28% cut into the Arbuckle Group and approximately 23% continue upward into post-Arbuckle sedimentary units. We suggest that the presence of these through-going faults make it possible for conduction of fluids between the sedimentary cover and the Precambrian basement. Thus, our findings in this study provide insight into the influence of the long-lived Nemaha structure on the deformation of the basement of north-central Oklahoma.

## Acknowledgments

We would like to thank the Osage Nation of Oklahoma and Spyglass Energy LLC for providing the seismic data and allowing them to be published. We also would like to thank L. Horne and two anonymous reviewers for their constructive reviews, which helped improve the quality of this paper. The University of Oklahoma provides access to numerous computational and visualization software packages. Petrel was used to interpret the volumes and create the images of the time horizons and vertical seismic slices. AASPI was used to generate the attributes that are paramount in the interpretation of the surfaces. The rose diagram displayed in the study was generated with GEOrient software.

## Data and materials availability

The 3D seismic surveys were provided by the Osage Nation and Spyglass LLC. Fault orientation and vertical separation data can be obtained by contacting the corresponding author. Supplementary information can be accessed through the following link: http://dx.doi.org/10/1190/INT-2014-0026.2.

## References

AASPI, 2019, Attribute-assisted seismic processing and interpretation software documentation, http://mcee.ou.edu/aaspi/documentation.html, accessed August 2019.

Alt, R. C., and M. D. Zoback, 2017, In situ stress and active faulting in Oklahoma: Bulletin of the Seismological Society of America, **107**, 216–228, doi: 10.1785/0120160156.

Anderson, J. L., 1983, Proterozoic anorogenic granite plutonism of North America: Geological Society of America Memoirs Proterozoic Geology: Selected Papers from an International Proterozoic Symposium, 133–54.

Bahorich, M., and S. Farmer, 1995, 3-D seismic discontinuity for faults and stratigraphic features: The coherence cube: The Leading Edge, **14**, 1053–1058, doi: 10.1190/1.1437077.

Barbour, A. J., J. H. Norbeck, and J. L. Rubinstein, 2017, The effects of varying injection rates in Osage County, Oklahoma, on the 2016Mw 5.8 Pawnee Earthquake: Seismological Research Letters **88**, 1040–1053, doi: 10.1785/0220170003.

Bickford, M. E., K. L. Harrower, W. J. Hoppe, B. K. Nelson, R. L. Nusbaum, and J. J. Thomas, 1981, Rb-Sr and U-Pb geochronology and distribution of rock types in the Precambrian basement of Missouri and Kansas: Geological Society of America Bulletin, **92**, 323–341, doi: 10.1130/0016-7606(1981)92<323:RAUGAD>2.0.CO;2.

Bickford, M. E., W. R. Van Schmus, K. E. Karlstrom, P. A. Mueller, and G. D. Kamenov, 2015, Mesoproterozoic-trans-laurentian magmatism: A synthesis of continent-wide age distributions, New SIMS U–Pb Ages, zircon saturation temperatures, and Hf and Nd isotopic compositions: Precambrian Research, **265**, 286–312, doi: 10.1016/j.precamres.2014.11.024.

Burke, K., and J. F. Dewey, 1973, Plume-generated triple junctions: Key indicators in applying plate tectonics to old rocks: The Journal of Geology, **81**, 406–433, doi: 10.1086/627882.

Carroll, H. B., K. C. Chen, G. Guo, W. I. Johnson, T. K. Reeves, and B. Sharma, 1999, Exploration 3-D seismic field test/native tribes initiative: National Petroleum Technology Office.

Cartwright, J., and D. M. Hansen, 2006, Magma transport through the crust via interconnected sill complexes: Geology, **34**, 929–932, doi: 10.1130/G22758A.1.

Chang, K. W., and P. Segall, 2016, Injection-induced seismicity on basement faults including poroelastic

Downloaded 10/26/20 to 12.233.159.194. Redistribution subject to SEG license or copyright; see Terms of Use at https://library.seg.org/page/policies/terms
DOI:10.1190/INT-2020-0053.1

stressing: Journal of Geophysical Research, Solid Earth, **121**, 2708–2726, doi: 10.1002/2015JB012561.

Chopra, S. J., L. J. Infante-Paez, and K. J. Marfurt, 2018, Intra-basement intrusions in the STACK area of Oklahoma, Search and Discovery 42229, http://mcee.ou.edu/aaspi/publications/2018/Chopra_et_al_2018-Intra-basement_intrusions_in_the_STACK_area_of_Oklahoma.pdf, accessed April 2019.

Chopra, S. J., and K. J. Marfurt, 2007, Seismic attributes for prospect identification and reservoir characterization: SEG.

Crain, K. D., and J. C. Chang, 2018, Elevation map of the top of the crystalline basement in Oklahoma and surrounding states, OGS Open-File Report 1-2018, http://ogs.ou.edu/docs/openfile/OF1-2018.pdf, accessed November 2019.

Crone, A. J., and K. V. Luza, 1990, Style and timing of holocene surface faulting on the meers fault, Southwestern Oklahoma: Geological Society of America Bulletin **102**, 1–17, doi: 10.1130/0016-7606(1990)102<0001:SATOHS>2.3.CO;2.

Denison, R. E., 1966, Basement rocks in adjoining parts of Oklahoma, Kansas, Missouri, and Arkansas: PhD dissertation, University of Texas.

Denison, R. E., 1981, Basement Rocks in Northeastern Oklahoma, Oklahoma Geological Survey, 84, http://www.ogs.ou.edu/pubsscanned/Circulars/circular84mm.pdf, accessed November 2019.

Elebiju, O. O., S. Matson, G. R. Keller, and K. J. Marfurt, 2011, Integrated geophysical studies of the basement structures, the Mississippi Chert, and the Arbuckle Group of Osage County Region, Oklahoma: AAPG Bulletin, **95**, 371–393, doi: 10.1306/08241009154.

Ellsworth, W. L., 2013, Injection-induced earthquakes: Science, **341**, 1225942, doi: 10.1126/science.1225942.

Ellsworth, W. L., A. L. Llenos, A. F. Mcgarr, A. J. Michael, J. L. Rubinstein, C. S. Mueller, M. D. Petersen, and E. Calais, 2015, Increasing seismicity in the U.S. midcontinent: Implications for earthquake hazard: The Leading Edge, **34**, 618–626, doi: 10.1190/tle34060618.1.

Elmore, R. D., P. K. Sutherland, and P. B. White, 1990, Middle Pennsylvanian recurrent uplift of the Ouachita fold belt and basin subsidence in the Arkoma Basin, Oklahoma: Geology, **18**, 906–909, doi: 10.1130/0091-7613(1990)018<0906:MPRUOT>2.3.CO;2.

Gay, S., 2003, The Nemaha trend — a system of compressional thrust-fold, strike-slip structural Features in Kansas and Oklahoma, Part 1: Shale Shaker **51**, 9–17.

Guo, G., and S. A. George, 1999, An analysis of surface and subsurface lineaments and fractures for oil and gas exploration in the Mid-Continent Region: Fossil Disclaimer, 1–48.

Hatcher, R. D., Jr, 2010, The Appalacian Orogen: A brief summary *in* R. P. Tollo, M. J. Batholomew, J. P. Hibbard, and PM. Karabinos, eds., From Rodinia to Pangea: The lithotectonic record of the Appalachian region: Geological Society of America Memoir, **206**, 1–19.

Hinze, W. J., D. J. Allen, L. W. Braile, and J. Mariano, 1997, The midcontinent rift system: A major proterozoic continental rift: Geological Society of America: Special Paper, **312**, 7–35.

Holland, A. A., 2013, Optimal fault orientations within Oklahoma: Seismological Research Letters, **84**, no. 5, 876–890, doi: 10.1785/0220120153.

Jacobs, T., 2016, Seismic shifts in Oklahoma lead to stricter regulations: Journal of Petroleum Technology, **68**, 44–48, doi: 10.2118/0516-0044-JPT.

Johnson, K. S., 1996, Geology of Oklahoma, *in* K. S. Johnson and N. H. Suneson, Rockhounding and earth-science Activities in Oklahoma, 1995 Workshop: Oklahoma Geological Survey Special Publication **96**, no. 5.

Keller, G. R., and R. A. Stephenson, 2007, The Southern Oklahoma and Dniepr-Donets Aulacogens: A comparative analysis: Geological Society of America Memoirs 4-D Framework of Continental Crust, 127–43.

Keranen, K. M., M. Weingarten, G. A. Abers, B. A. Bekins, and S. Ge, 2014, Sharp increase in Central Oklahoma seismicity since 2008 induced by massive wastewater injection: Science **345**, 448–451, doi: 10.1126/science.1255802.

Kibikas, W. M., B. M. Carpenter, and A. Ghassemi, 2019, The petrophysical and mechanical properties of Oklahoma's crystalline basement: 53rd US Rock Mechanics/Geomechanics Symposium: American Rock Mechanics Association.

Kluth, C. F., 1986, Plate tectonics of the ancestral rocky mountains: AAPG Memoir, 41.

Kolawole, F., C. S. Johnston, C. B. Morgan, J. C. Chang, K. J. Marfurt, D. A. Lockner, Z. Reches, and B. M. Carpenter, 2019, The susceptibility of Oklahoma's basement to seismic reactivation: Nature Geoscience, **12**, 839–844, doi: 10.1038/s41561-019-0440-5.

Kolawole, F., M. Simpson Turko, and B. M. Carpenter, 2020, Basement-controlled deformation of sedimentary sequences, Anadarko Shelf, Oklahoma: Basin Research.

Kroll, K. A., E. S. Cochran, and K. E. Murray, 2017, Poroelastic properties of the Arbuckle Group in Oklahoma derived from well fluid level response to the 3 September 2016Mw 5.8 Pawnee and 7 November 2016 Mw 5.0 Cushing Earthquakes: Seismological Research Letters, **88**, 963–970, doi: 10.1785/0220160228.

Lidiak, E. G., 1996, Geochemistry of subsurface proterozoic rocks in the Eastern Midcontinent of the United States: Further evidence for a within-plate tectonic setting: Basement and Basins of Eastern North America, **308**, 45–66, doi: 10.1130/0-8137-2308-6.45.

Liner, K. M., 2015, An investigation of 3D seismic deep basement events in Osage County, Oklahoma: M.S. thesis, University of Oklahoma.

Luza, K. V., 2008, Earthquakes of Oklahoma, Oklahoma Geological Survey. Educational Publication, 9, p. 9.

Luza, K. V., and J. E. T. Lawson Jr., 1983, Seismicity and tectonic relationships of the Nemaha Uplift in Oklahoma, Part V. Final report: Technical Report, NUREG/CR-3109ON: DE83901537, https://www.osti.gov/biblio/6372925-seismicity-tectonic-relationships-nemaha-uplift-oklahoma-part-final-report, accessed August 2019

Magee, C., J. D. Muirhead, A. Karvelas, S. P. Holford, C. A. l. Jackson, I. D. Bastow, N. Schofield, C. T. Stevenson, C. McLean, W. McCarthy, and O. Shtukert, 2016, Lateral magma flow in mafic sill complexes: Geosphere, **12**, 809–841, doi: 10.1130/GES01256.1.

Mai, H. T., O. O. Elebiju, and K. J. Marfurt, 2014, Attribute illumination of basement faults, Examples from Cuu Long basin basement, Vietnam and the Midcontinent, USA: Interpretation, **2**, no. 1, SA119–SA126, doi: 10.1190/INT-2013-0091.1.

McBee, W., 2003, The Nemaha and other strike-slip faults in the Midcontinent U.S.A.: Midcontinent Section Meeting (Tulsa), http://archives.datapages.com/data/tgs/tgs-sp/data/051/051001/59_tgs-sp0510059.htm, accessed March 2019

Mohammadi, S., J. M. Gregg, K. L. Shelton, M. S. Appold, and J. O. Puckette, 2019, Influence of late diagenetic fluids on Mississippian carbonate rocks on the Cherokee–Ozark Platform, Northeast Oklahoma, Northwest Arkansas, Southwest Missouri, and Southeast Kansas: Mississippian Reservoirs of the Midcontinent, 323–352.

Moores, E. M., 1991, Southwest U.S.-East Antarctic (SWEAT) connection: A hypothesis: Geology **19**, 425–428, doi: 10.1130/0091-7613(1991)019<0425:SUSEAS>2.3.CO;2.

Nelson, R., T. Patton, and C. Morley, 1992, Rift-segment interaction and its relation to hydrocarbon exploration in continental rift systems: AAPG Bulletin, **76**, 1153–1169, doi: 10.1306/BDFF898E-1718-11D7-8645000102C1865D.

Northcutt, R. A., and J. A. Campbell, 1995, Geologic provinces of Oklahoma: Oklahoma Geological Survey open file report 5, http://ogs.ou.edu/docs/openfile/OF5-95.pdf, accessed March 2019

Perry, W. J., Jr., 1989, Tectonic evolution of the Anadarko Basin Region, Oklahoma: U.S. Geological Survey.

Pollyea, R. M., M. C. Chapman, R. S. Jayne, and H. Wu, 2019, High density oilfield wastewater disposal causes deeper, stronger, and more persistent earthquakes: Nature Communications, **10**, 1–10, doi: 10.1038/s41467-019-11029-8.

Qin, Y., X. Chen, J. I. Walter, J. Haffener, D. T. Trugman, B. M. Carpenter, M. Weingarten, and F. Kolawole, 2019, Deciphering the stress state of seismogenic faults in Oklahoma and southern Kansas based on an improved stress map: Journal of Geophysical Research: Solid Earth, **124**, 12920–12934, doi: 10.1029/2019jb018377.

Schoenball, M., and W. L. Ellsworth, 2017, Waveform-relocated earthquake catalog for Oklahoma and southern Kansas illuminates the regional fault network: Seismological Research Letters, **88**, 1252–1258, doi: 10.1785/0220170083.

Schwab, D. R., T. S. Bidgoli, and M. H. Taylor, 2017, Characterizing the potential for injection-induced fault reactivation through subsurface structural mapping and stress field analysis, Wellington Field, Sumner County, Kansas: Journal of Geophysical Research: Solid Earth, **122**, 10132–10154, doi:10.1002/2017jb014071.

Segall, P., and S. Lu, 2015, Injection-induced seismicity: Poroelastic and earthquake nucleation effects: Journal of Geophysical Research: Solid Earth, **120**, 5082–5103, doi: 10.1002/2015jb012060.

Shah, A. K., and G. R. Keller, 2017, Geologic influence on induced seismicity: Constraints from potential field data in Oklahoma: Geophysical Research Letters, **44**, 152–161, doi: 10.1002/2016GL071808.

Sims, P. K., 1985, Precambrian basement map of the Northern Midcontinent, U.S.A.: Open-File Report, 85, no. 0604.

Slagstad, T., N. G. Culshaw, J. S. Daly, and R. A. Jamieson, 2009, Western Grenville province holds key to Midcontinental Granite-Rhyolite Province Enigma: Terra Nova, **21**, 181–187, doi: 10.1111/j.1365-3121.2009.00871.x.

Stein, C. A., S. Stein, M. Merino, G. R. Keller, L. M. Flesch, and D. M. Jurdy, 2014, Was the Midcontinent rift part of a successful seafloor-spreading episode?: Geophysical Research Letters, **41**, 1465–1470, doi: 10.1002/2013GL059176.

Thomas, J. J., R. D. Shuster, and M. E. Bickford, 1984, A terrane of 1,350- to 1,400-M.y.-old silicic volcanic and plutonic rocks in the buried proterozoic of the mid-continent and in the Wet Mountains, Colorado: Geological Society of America Bulletin, **95**, 1150–1157, doi: 10.1130/0016-7606(1984)95<1150:ATOTMS>2.0.CO;2.

Walsh, F. R., and M. D. Zoback, 2016, Probabilistic assessment of potential fault slip related to injection-induced earthquakes: Application to North-Central Oklahoma, USA: Geology, **44**, 991–994, doi: 10.1130/G38275.1.

Yeck, W. L., G. P. Hayes, D. E. Mcnamara, J. L. Rubinstein, W. D. Barnhart, P. S. Earle, and H. M. Benz, 2017, Oklahoma experiences largest earthquake during ongoing regional wastewater injection hazard mitigation efforts: Geophysical Research Letters, **44**, 711–717, doi: 10.1002/2016GL071685. .

Zhai, G., M. Shirzaei, M. Manga, and X. Chen, 2019, Pore-pressure diffusion, enhanced by poroelastic stresses, controls induced seismicity in Oklahoma: Proceedings of the National Academy of Sciences, **116**, 16228–16233, doi: 10.1073/pnas.1819225116.

---

Biographies and photographs of the authors are not available.

Downloaded 10/26/20 to 12.233.159.194. Redistribution subject to SEG license or copyright; see Terms of Use at https://library.seg.org/page/policies/terms
DOI:10.1190/INT-2020-0053.1